Journal of Intelligent & Robotic Systems (2018) 91:115–131
https://doi.org/10.1007/s10846-018-0870-0

Path Planning Generation Algorithm for a Class of UAV Multirotor Based on State of Health of Lithium Polymer Battery

R. Schacht-Rodríguez[1,2] · J.-C. Ponsart[2] · C.-D. García-Beltrán[1] · C.-M. Astorga-Zaragoza[1] · D. Theilliol[2] · Y. Zhang[3]

Received: 25 April 2018 / Accepted: 9 May 2018 / Published online: 2 June 2018

Abstract

Nowadays, it exists path planning strategies dedicated to generate trajectories considering different navigation issues in UAV multirotors, such as 3D navigation in cluttered and uncluttered environments, obstacle avoidance, and path re-planning. Such path generators are mainly based on the dynamics associated to position and orientation of the UAV, and the attenuation of external disturbances as the wind. However, one of the main limitations of these methods is that they do not take into account the relationship between the path planning task and the energy consumption associated with the battery performance or State of Health (SoH). In this work, a path planning generation algorithm that take into account the evolution of the battery performance is presented. First, the computation of the battery SoH is realized by introducing two degradation models. Subsequently, the path planning algorithm is defined as a multi-objective optimization problem where the objective is to find a feasible trajectory between way-points whiles minimizing the energy consumed and the mission final time depending on the variation of the battery SoH. Finally, the proposed path planning algorithm is compared with a *classical* path generation method based on polynomial functions to evaluate the minimization of the energy consumption. The simulation results demonstrate that the proposed path planning algorithm is able to generate feasible and minimum energy trajectories despite the constraints in the battery SoH.

Keywords UAV · Path planning · Energy minimization · Lithium batteries · State of health · Optimization

1 Introduction

Recent advances in the development of Unmanned Aerial Vehicle multirotors powered by Lithium Polymer batteries have made it possible to extend its use in a variety of civilian applications. In these applications, the UAV is used as a data source to carry out inspection, surveillance, and mapping tasks by developing autonomous or semi-autonomous flight mission [1], e.g. monitoring of crops and forest [2], exploring of archaeological areas [3, 4], monitoring of geothermal environments [5], surveillance [6] and topography studies [7]. Usually, the mission for such applications is defined as the UAV navigation through a set of paths connected by n targets or way-points inside a limited workspace which can be known or unknown. In addition, path planning task consists of determining the *adequate path* to connect the ways-points satisfying *the mission requirements* and *the physical constraints* of the UAV [8]. The mission requirements can be considered as the minimum and maximum altitude and flight speed, the maximum flight endurance and minimum energy to fulfill the mission. Likewise, the physical constraints of the UAV are mainly associated to the minimum and maximum orientation and control inputs, and minimum battery voltage. Such requirements are linked to the UAV application and define the path characteristics that the UAV has to track.

According to [9], the main issues that a path planning algorithm for UAV multirotors must consider are: the autonomous navigation in three dimensions (3D) inside a cluttered or uncluttered environment, the obstacle avoidance, and the dynamical constraints of the UAV. In order

This work was supported by CONACyT (Consejo Nacional de Ciencia y Tecnología.

✉ J.-C. Ponsart
Jean-Christophe.Ponsart@univ-lorraine.fr

Extended author information available on the last page of the article.

to solve such issues, different path planning algorithms have been developed. In [10], a path planning algorithm for autonomous robotic exploration and inspection based on an on-line planning method in a receding horizon fashion by sampling possible future configuration in geometric random tree was introduced. The authors in [11] presented a method to path definition based on a Cascaded control architecture and using a nonlinear control technique for both control loops (position and attitude) taking into account obstacles perceived in real-time and avoids collisions. In [12], the authors focused on the analysis of different algorithms dedicated to path planning considering the flight time and the distance traveled from one point to another and evaluating the autonomously avoiding obstacles. In [13], an algorithm for trajectory generation based on the differentially flat quadrotor model through complex real-world environments with an optimizing polynomial path segments was presented. As it can be noticed, in these works the path planning is developed with the consideration of the trajectory characteristics and the UAV dynamics constraints. However, they do not take into account the dependency between the energy consumed during the flight and the battery performance. In this work we are focused on path planning algorithms dedicated to minimize the energy consumption.

1.1 Related Work

One way to consider the dependency between energy consumed during the flight and the battery performance is to determine the maximum flight endurance. According to [14], the flight endurance is mainly determinate by two power-related factors: the required power to sustain the desired flight profile and the battery discharge performance. The power required is associated to the total energy necessary to take-off, move between way-points and landing, i.e the elements which define the trajectory, and the battery discharge performance which depends on the actual condition of the battery or State of Health (SoH) and determine the battery aging rate. The battery aging is mainly caused by two factors: the storage and the use (cyclic charge/discharge) [15]. However, other factors contribute to increase the battery aging such as deep discharges, inadequate charging methods, and operating temperature variations. In that sense, it is necessary to quantify the battery aging by defining the SoH between flights in order to use this information in a complete path planning strategy to guarantee the fulfillment of the mission and the UAV integrity.

Different solutions have been presented to overcome the problems associated with the path planning based on energy supplied. Such solutions have focused into generate strategies to optimize the energy consumption, and improve the efficiency of the flight performance considering two approaches: mechanics and analytics. The mechanics approaches are associated to geometric characteristics of the UAV, e.g in [16] an experimental platform based on quadrotor was designed to maximize the thrust using an aero-elastic blade design was presented. In [17], the authors introduce a four-rotor configuration that merges the simplicity of a quadrotor with the energy efficiency of a helicopter, while improving maneuvering rotor bandwidth. The authors in [18] conceived a compound multirotor configuration specifically for flight through narrow corridors, and the design combines the contradictory requirements of limited width, high agility and long endurance while carrying a significant payload. On the other hand, the analytics approaches are dedicated to generate optimal path planning or flight profiles, e.g. in [19], a path planning method based on two optimal control with respect to the angular accelerations of the motor for a quadrotor is presented, and the solution was yielded in to find minimum energy and fixed-energy paths. In [20] was presented the results of an analysis of the energy consumption in various discrete movement states of a multirotor. A systematic relationship between the system and movement parameters and the energy consumption was established, and finally a generic energy consumption profile model was generated and validated. The authors in [21] investigated three prominent types of smooth trajectories (minimum acceleration, minimum jerk and minimum snap), and evaluate their energetic efficiency through the total energy consumption. The energy consumed by each trajectory type was determined via aerodynamics-based expressions for power consumption of rotorcraft. In [22], a flatness-based flight trajectory planning/re-planing strategy considering the occurrence of faults in actuators is presented, and the trajectory planning/re-planning problem is formulated as a constrained optimization problem. As it can be seen, different analytically solutions have been proposed to address the path planning problem along the energy consumption. However, these works do not take into account the influence of the battery performance and the variations of SoH in the path planning problem. In that sense, our work introduces a path planning algorithm that takes into account the degradation of the battery performance by evaluating the battery SoH considering degradation models related to battery parameters. The degradation models are obtained through experimental data from a degraded battery cell. Then, the path planning problem is defined within the framework of optimal control as a minimization problem of the consumed energy during the flight as well as the final time. The minimization of the energy and the final time considering the battery performance makes it is possible to extend the flight endurance and to guaranty the fulfillment of the mission. On the other hand, the quantification of the battery health and the use of this information in the path

planning algorithm, helps to determine the appropriate battery replacement time. Taking into account the aforementioned elements, main contributions of this study are the following:

1. The analysis of the main aging modes in Lithium Polymer batteries and computation of State of Health by degradation models,
2. The development of a complete path planning algorithm based on the dependency of the battery performance,
3. The minimization of the energy consumption and the mission final time t_f considering the constraints associated with the UAV dynamics and the variations of the battery State of Health by considering a constrained optimization problem,
4. The maximization of the flight endurance by generating minimum - energy paths.

The proposed algorithm is compared with a *classical* path planning method based on polynomial functions considering an UAV hexacopter. The simulation results demonstrate that the proposed path planning algorithm is able to generate trajectories despite the variations in the battery SoH and that the energy consumed is minimized.

1.2 Outline

This paper is organized as follows: The dynamics of the hexacopter and the propulsion system (Li-Po battery and BrushLess DC Motors) are introduced in Section 2. The considerations about the battery SoH and the computation of the degradation models are explained in Section 3. The path planning generations algorithm is defined in Section 4. In Section 5 the simulation results are presented. Finally the conclusions and future works are described in Section 6.

2 Mathematical Model of UAV Hexacopter

In this Section the dynamics of the hexacopter and the elements that compose the propulsion system (lithium battery and motors) are described.

2.1 Hexacopter Dynamics

The considered hexacopter is composed by six BrushLess DC Motors (BLDCMs) attached to a rigid and symmetrical six-arm frame as it can be seen in Fig. 1. In turn, each BLDCM has a rigid propeller connected to its rotor and generates a positive thrust f_i and torques τ_i, $i = 1, \cdots, 6$, proportionally to the square angular speed of the propeller. The sum of the individuals forces produces the total thrust T_{thr} to lift, and the difference generates the torques acting on the hexacopter. Moreover, the BLDCMs 1, 3, and 5 rotate in clockwise whiles BLDCMs 2, 4, and 6 rotate in counterclockwise given the so-called "*X*" configuration. Such configuration allows to cancel gyroscopic effects and aerodynamic torques. The movement of the hexacopter is performed around two reference frames: the fixed inertial frame, denoted by E_e (hexacopter position), and the non-inertial frame or rigid body frame, denoted by E_b (hexacopter orientation), and assuming that the non-inertial frame coincides with the center of gravity of the hexacopter. By adopting the Euler angles parametrization the orientation of the hexacopter in the space is given by the rotation from E_b to E_e by the rotation matrix $\mathbf{R}(\phi, \theta, \psi) \in SO(3)$ defined as:

$$\mathbf{R} = \begin{bmatrix} \mathbf{c}\psi\mathbf{c}\theta & \mathbf{c}\psi\mathbf{s}\theta\mathbf{s}\phi - \mathbf{s}\psi\mathbf{c}\phi & \mathbf{c}\psi\mathbf{s}\theta\mathbf{c}\phi + \mathbf{s}\psi\mathbf{s}\phi \\ \mathbf{s}\psi\mathbf{c}\theta & \mathbf{s}\psi\mathbf{s}\theta\mathbf{s}\phi + \mathbf{c}\psi\mathbf{c}\phi & \mathbf{s}\psi\mathbf{s}\theta\mathbf{c}\phi - \mathbf{c}\psi\mathbf{c}\phi \\ -\mathbf{s}\theta & \mathbf{c}\theta\mathbf{c}\phi & \mathbf{c}\theta\mathbf{c}\phi \end{bmatrix}, \quad (1)$$

where $\mathbf{c}$ and $\mathbf{s}$ are the trigonometric functions cos and sin respectively. By considering the Newton-Euler formalism, the dynamic of the hexacopter considered as a rigid body under external forces applied to the center of mass expressed on the non-inertial frame is expressed as [23, 24]:

$$\begin{aligned} \dot{\xi} &= v \\ m\dot{v} &= f \\ \dot{R} &= R\hat{\bar{\omega}} \\ I\dot{\bar{\omega}} &= -\bar{\omega} \times I\bar{\omega} + \tau, \end{aligned} \quad (2)$$

where $\xi = [x\ y\ z]^{\mathrm{T}} \in \mathbb{R}^3$ is the position of the hexacopter with respect to the inertial frame E_e relative to a fixed origin, $v \in E_e$ is the linear velocity expressed in the inertial frame, $\bar{\omega} \in E_b$ is the angular velocity of the hexacopter expressed in the body frame E_b, m is the total mass, $I \in \mathbb{R}^{3\times3}$ denotes the constant inertia matrix around the center of mass, $\hat{\bar{\omega}}$ is the skew-symmetric matrix of the vector $\bar{\omega}$. $f \in E_e$ is the vector of the principal non-conservative forces and includes the thrust T_{thr} and drag terms associated with the BLDCMs. $\tau \in E_b$ is derived from differential thrust associated with pairs of BLDCMs along with aerodynamics effects and gyroscopic effects.

Translational and Gravitational Forces The forces acting on the hexacopter are given by the translational force T_{thr} and the gravitational force g. The translational force is defined as:

$$T_{thr} = \sum_{i=1}^{6} f_i, \quad (3)$$

where the thrust f_i produced by the ith-BLDCM in free air is modeled as $f_i = b\omega_i^2$ in the z-direction, where $b > 0$ is a constant associated to propeller geometry and ω_i is the

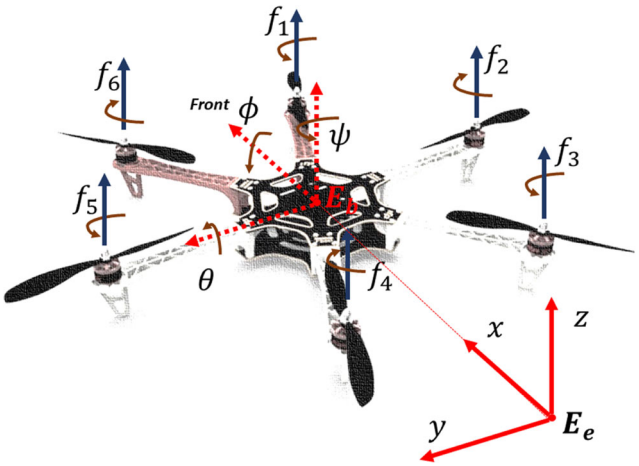

Fig. 1 Reference frames of the UAV hexacopter

angular speed of the ith-BLDCM. In that sense, Eq. 3 is rewritten as:

$$T_{thr} = b\left(\sum_{i=1}^{6}\omega_i^2\right), \tag{4}$$

and the gravitational force applied to the hexacopter is:

$$f_g = -mgE(3), \tag{5}$$

where $E(3) = [0\,0\,1]^{\mathrm{T}}$ is an unitary vector in E_e. Finally, the force applied to hexacopter is defined as:

$$F = R_{E(3)}T_{thr} + f_g, \tag{6}$$

where $R_{E(3)} = \mathbf{R}E(3)$, with $\mathbf{R}$ as the rotation matrix (1).

Torques The torque generated by each BLDCM is denoted by τ_{BLDCMi}, moreover the torque of the BLDCM is opposed by an aerodynamic drag $\tau_d = d\omega_i^2$, where $b > 0$ is a constant associated for the quasi-stationary maneuvers (near hover) in free flight. In a steady stable condition, i.e. $\dot{\omega}_i = 0$ it it is assumed that $\tau_{BLDCMi} = \tau_d$ and the generalized torques considering the hexacopter geometry are defined as:

$$\tau\left(E_b\right) = \begin{bmatrix} \frac{bl}{2}\left(-\omega_1^2 - 2\omega_2^2 - \omega_3^2 + \omega_4^2 + 2\omega_5^2 + \omega_6^2\right) \\ \frac{bl\sqrt{3}}{2}\left(-\omega_1^2 + \omega_3^2 + \omega_4^2 - \omega_6^2\right) \\ d\left(-\omega_1^2 + \omega_2^2 - \omega_3^2 + \omega_4^2 - \omega_5^2 + \omega_6^2\right) \end{bmatrix}, \tag{7}$$

where $\tau\left(E_b\right) = \left[\tau_\phi\ \tau_\theta\ \tau_\psi\right]^{\mathrm{T}}$ are the generalized torques around roll, pitch and yaw movements, l is the distance from each BLDCM to the center of mass of the hexacopter, and $c = \sqrt{3}$ is a constant associated with hexacopter geometry. It is also assumed that each rotor can be considered as a rigid disc rotating around the z-axis in the body frame with angular speed ω_i, and furthermore the rotary shaft of the rotor is considered itself moving with the angular speed of the frame, which leads to gyroscopic torques applied to the hexacopter:

$$\tau_{G_b} = -\left(\bar{\omega} \times E(3)\right)\sum_{i=1}^{n} J_m\omega_i, \tag{8}$$

where J_m is the inertial of the rotor. Finally the differential thrust associated with the torques is expressed as:

$$\tau = \tau\left(E_b\right) + \tau_{G_b}. \tag{9}$$

By considering the Eqs. 6 and 9, the system (2) is rewriting as

$$\begin{aligned} \dot{\xi} &= v \\ m\dot{v} &= R_{E(3)}T_{thr} - mgE(3) \\ \dot{R} &= R\hat{\bar{\omega}} \\ I\dot{\bar{\omega}} &= -\bar{\omega} \times I\bar{\omega} + \tau\left(E_b\right) + \tau_{G_b}. \end{aligned} \tag{10}$$

In order to express the final representation of the model describing the dynamics of hexacopter movement in the inertial and rigid body reference frames, the system (2) is separated into position dynamics (denoted as ξ) and dynamics orientation (denoted as η). In that sense, the system (2) with respect to ξ is defined as

$$\ddot{\xi} = \frac{1}{m}\left(\mathbf{R}E(3)T_{thr} - mgE(3)\right) \tag{11}$$

where

$$\mathbf{R}E(3) = \begin{bmatrix} \mathbf{s}\phi\mathbf{s}\psi + \mathbf{c}\phi\mathbf{c}\psi\mathbf{s}\theta \\ \mathbf{c}\phi\mathbf{s}\psi\mathbf{s}\theta - \mathbf{c}\psi\mathbf{s}\phi \\ \mathbf{c}\theta\mathbf{c}\phi \end{bmatrix} \tag{12}$$

and defining $U_1 = T_{thr}$ the following equation system describing the hexacopter position around $x - y - z$ axis is obtained:

$$\begin{aligned} \ddot{x} &= \left(\mathbf{c}\phi\mathbf{s}\theta\mathbf{c}\psi + \mathbf{s}\phi\mathbf{s}\psi\right)\frac{U_1}{m} \\ \ddot{y} &= \left(\mathbf{c}\phi\mathbf{s}\theta\mathbf{s}\psi - \mathbf{s}\phi\mathbf{c}\psi\right)\frac{U_1}{m} \\ \ddot{z} &= -g + \left(\mathbf{c}\phi\mathbf{c}\theta\right)\frac{U_1}{m}. \end{aligned} \tag{13}$$

Likewise, the equation system describing the hexacopter orientation around Euler angles is obtained by considering that $\bar{\omega} \approx \dot{\eta}$, $\tau_\phi = U_2$, $\tau_\theta = U_3$, and $\tau_\psi = U_4$ as follows

$$\begin{aligned} \ddot{\phi} &= \frac{I_y - I_z}{I_x}\dot{\theta}\dot{\psi} + \frac{J_m}{I_x}\omega_G\dot{\theta} + \frac{U_2}{I_x} \\ \ddot{\theta} &= \frac{I_z - I_x}{I_y}\dot{\phi}\dot{\psi} - \frac{J_m}{I_y}\omega_G\dot{\phi} + \frac{U_3}{I_y} \\ \ddot{\psi} &= \frac{I_x - I_y}{I_z}\dot{\theta}\dot{\phi} + \frac{U_4}{I_z}, \end{aligned} \tag{14}$$

where I_x, I_y and I_z are the inertial moments around the $x - y - z$ axis, respectively. ω_G is the gyroscopic effect (8). According to Eqs. 6 and 9, the inputs of the system are defined as:

$$\begin{aligned} U_1 &= b\left(\omega_1^2 + \omega_2^2 + \omega_3^2 + \omega_4^2 + \omega_5^2 + \omega_6^2\right) \\ U_2 &= \frac{bl}{2}\left(-\omega_1^2 - 2\omega_2^2 - \omega_3^2 + \omega_4^2 + 2\omega_5^2 + \omega_6^2\right) \\ U_3 &= \frac{bl\sqrt{3}}{2}\left(-\omega_1^2 + \omega_3^2 + \omega_4^2 - \omega_6^2\right) \\ U_4 &= d\left(-\omega_1^2 + \omega_2^2 - \omega_3^2 + \omega_4^2 - \omega_5^2 + \omega_6^2\right) \\ \omega_G &= -\omega_1 + \omega_2 - \omega_3 + \omega_4 - \omega_5 + \omega_6^2 \end{aligned} \tag{15}$$

Finally, the systems (13) and (14) can be written in a state space form $\dot{X} = f(X, U)$ as

$$\dot{X} = f(X,\ U) = \begin{bmatrix} x_2 \\ (\mathbf{c}x_7\mathbf{s}x_9\mathbf{c}x_{11} + \mathbf{s}x_7\mathbf{s}x_{11})\frac{U_1}{m} \\ x_4 \\ (\mathbf{c}x_7\mathbf{s}x_9\mathbf{s}x_{11} - \mathbf{s}x_7\mathbf{c}x_{11})\frac{U_1}{m} \\ x_6 \\ -g + (\mathbf{c}x_7\mathbf{c}x_9)\frac{U_1}{m} \\ x_8 \\ \frac{I_y - I_z}{I_x}\dot{x}_{10}\dot{x}_{12} + \frac{J_m}{I_x}\omega_G\dot{x}_{10} + \frac{U_2}{I_x} \\ x_{10} \\ \frac{I_z - I_x}{I_y}\dot{x}_8\dot{x}_{12} - \frac{J_m}{I_y}\omega_G\dot{x}_8 + \frac{U_3}{I_y} \\ x_{12} \\ \frac{I_x - I_y}{I_z}\dot{x}_8\dot{x}_{10} + \frac{U_4}{I_z} \end{bmatrix}, \quad (16)$$

where $X = \left[x\ \dot{x}\ y\ \dot{y}\ z\ \dot{z}\ \phi\ \dot{\phi}\ \theta\ \dot{\theta}\ \psi\ \dot{\psi}\right]^{\mathrm{T}} = [x_1\, x_2\, x_3\, x_4\, x_5\, x_6\, x_7\, x_8\, x_9\, x_{10}\, x_{11}\, x_{12}]^{\mathrm{T}}$ is the state vector, and $U = [U_1\, U_2\, U_3\, U_4]^{\mathrm{T}}$ is the input vector. Taking into account the system (16) with the inputs (15), and considering the yaw angle as $\psi \approx 0$ (assuming hover conditions) [25], neglecting the drag coefficients at low speeds, and decoupling the $x - y$ axes from z by supposing that $U_1 \approx g$, the following simplified linear model is obtained [22]:

$$\dot{\bar{X}} = A\bar{X} + BU = \begin{bmatrix} x_2 \\ g x_9 \\ x_4 \\ g x_7 \\ x_6 \\ -g + \frac{U_1}{m} \\ x_8 \\ \frac{U_2}{I_x} \\ x_{10} \\ \frac{U_3}{I_y} \\ x_{12} \\ \frac{U_4}{I_z} \end{bmatrix}, \quad (17)$$

where the A and B are compatible matrices. The simplified model (17) will be used in the Section 4.3 to develop the path tracking controller.

2.2 Propulsion System

The propulsion system of a UAV multirotor is composed by a set of BrushLess DC Motors (BLDCM) with a propeller attached to its rotor-shaft. The BLDCMs are powered by a Lithium Polymer battery through an Electronic Speed Control (ESC). In Fig. 2 the connection Li-Po battery - ESC - BLDCM is detailed for one motor. The ESC adjusts the angular speed of the BLDCM through a PWM signal. In this study the dynamic around the ESC is neglected and it is assumed that the voltage supply by the battery and the generated current by the motors are averaged with respect to the duty cycle value produced by the control signal.

2.2.1 Lithium Polymer battery dynamics

Lithium Polymer (Li-Po) batteries are devices converting the energy released by spontaneous chemical reaction to electricity work. Due to their rechargeable capability they belong to the Secondary Lithium batteries family and possess properties such as high discharge rate (C-rate), high energy and power densities. The Lithium Polymer (Li-Po) battery is made of several individual cells connected to each other in series (to have a high voltage value) or parallel (to have a high capacity in Ah) [26].

Electrical Submodel The battery model describes the mathematical relationship and evolution of voltage and State of Charge (SoC), which is the proportion of the charge available at a given time compared to the total charge available when the battery is fully charged. The range of the SoC is $SoC \in \left[0\ 1\right]$, where 1 corresponds to 100% of the charge, i.e the battery is fully charged, and 0

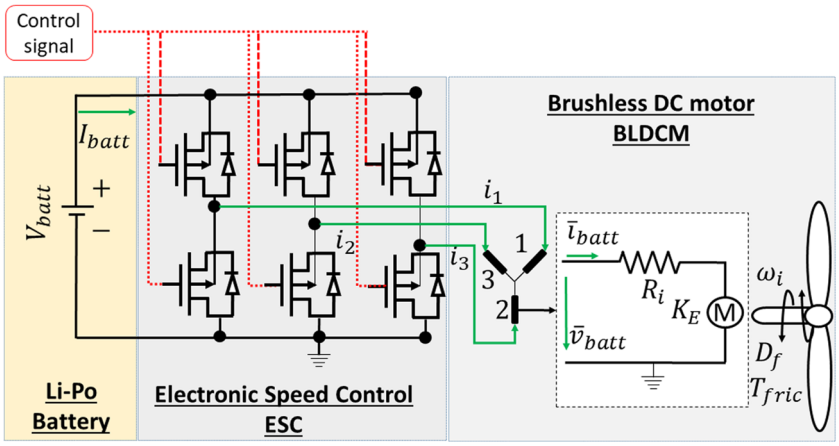

Fig. 2 Connexion of Li-Po battery - ESC - BLDCM

indicates that the battery is fully discharge, i.e. the End of Discharge (EoD) or cut-off voltage value has been reached. The mathematical model of the Li-Po battery is based on an Equivalent Circuit Representation (ECR) according to Fig. 3 [27]. In Fig. 3, (on the left-side of the circuit), the voltage $V_{SoC}(t)$ models the state of charge $SoC(t)$ of the battery from the capacity C_T. The voltage $V_{OCV}(V_{SoC})$ is the Open Circuit Voltage (OCV), i.e. it is the effective voltage in the battery terminals, and it is modeled as a function of the state of charge of the battery. The voltage $V_{R_{int}}(t)$ characterizes the ohmic over-potential due to the internal resistance of the battery R_{int}. $V_d(t)$ represents the transitory response of the voltage when a current is demanding to the battery. It is characterized by a first order response and its time constant depends on the value of parameters R_d and C_d. The mathematical model of the battery is given by:

$$\begin{aligned} \dot{V}_{SoC} &= -\frac{I_{batt}}{3600 \cdot C_T} \\ \dot{V}_d &= -\frac{V_d}{R_d \cdot C_d} + \frac{I_{batt}}{C_d} \\ V_{Batt} &= V_{OCV}(V_{SoC}) - V_d - R_{int}\, I_{batt}, \end{aligned} \tag{18}$$

where, the $V_{OCV}(V_{SoC})$ is experimentally defined as:

$$V_{OCV}(V_{SoC}) = \sum_{i=0}^{n} \lambda_i V_{SoC}^i + \ln(V_{SoC}) V_{SoC}. \tag{19}$$

n determines the order of the polynomial, and λ_i are the polynomial coefficients. It can be noted that the nonlinear function (19) is not unique and its formulation is obtained through experimental tests.

Thermal submodel. The temperature of the battery is modeled by the Newton's law of cooling [28], and it is assumed that the heat is generated and distributed uniformly in the battery:

$$\begin{aligned} Q_b &= R_{int} \cdot I_{batt}^2, \\ \dot{T}_{batt} &= \frac{hA}{c}(T_{air} - T_{batt}) + \frac{Q_b}{c}, \end{aligned} \tag{20}$$

where T_{batt} is the battery temperature, h is the heat transfer coefficient, A is the surface area of the battery, c is the heat capacity of the battery, T_{air} is the temperature of the cooling air, and Q_{batt} is the heat generated in the battery.

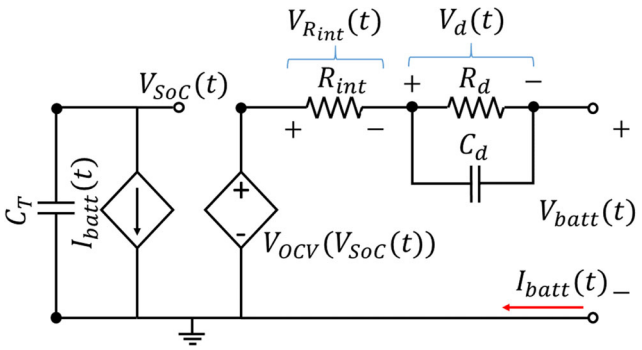

Fig. 3 Electrical equivalent circuit of Li-Po battery

2.2.2 BrushLess DC Motor Dynamics

The BrushLess DC motor is a type of permanent magnet synchronous motor. It is drive by a DC voltage source and a current commutation achieved by solid-state switches. The main advantages that render this type of motor suitable for aerial robotic applications are a long operating life, high dynamic response, better speed and torque characteristics and higher torque-weight ratio [29]. The mathematical model that describes the dynamics of the angular speed is divided into the electrical and the mechanical sub-models described by the following equations [30]:

$$\begin{aligned} \bar{v}_{batt_i} &= R\bar{i}_{batt_i} + K_E\omega_i, \\ \dot{\omega}_i &= \tfrac{1}{J_m}(K_E\bar{i}_{batt_i} - d\omega^2 - D_f\omega_i - T_{fric}), \end{aligned} \tag{21}$$

where $R = \frac{2}{3}(\sum_{j=1}^{3} R_j)$ is the equivalent electric resistance of each coil, K_E is the back electromotive force, ω_i is the angular velocity of the ith BLDCM, T_{fric} is the friction torque, D_f is the viscous damping coefficient, d is the drag constant, associated to the geometry of the propeller, and J_m is the inertia of the BLDCM. The average voltage $\bar{v}_{batt_i}$ and current $\bar{i}_{batt_i}(t)$ are the voltage and current generated by the ESC and they are computed as follows:

$$\begin{aligned} \bar{v}_{batt_i} &= V_{batt_i} \cdot Dc_i \\ I_{BLDCM_i} &= \bar{i}_{batt_i} \cdot Dc_i, \end{aligned} \tag{22}$$

where V_{batt} is the battery voltage, I_{BLDCM_i} is the current generated by the ith BLDCM and $I_{batt} = \sum_{i=1}^{6} I_{BLDCM_i}$. Dc_i is the duty cycle of Pulse-Width Modulation (PWM) signal, which corresponds to control signal of the BLDCM speed. $Dc_i \in [0\ 1]$ is defined as function of the reference angular speed of the ith-BLDCM and it is determined through experimental correlations, such as:

$$Dc_i = f(\omega_{ref_i}^2). \tag{23}$$

where $\omega_{ref_i}^2$ is the reference angular speed of the ith BLDCM.

3 Lithium Polymer Battery Health

In this Section, the principles of battery State of Health and the main mechanisms of aging are introduced. Subsequently, the degradation models are defined in Section 3.2.

3.1 State of Health

The battery State of Health describes the actual physical condition of the battery in comparison with its nominal condition [31], and it is established in a range between 0 and 1 $SoH \in [0\ 1]$, i.e. if $SoH = 1$ the battery is considered as new and $0 \leq SoH \leq 1$ the battery exhibits

an aging behavior. The decrease of the battery SoH is mainly due to two aging mechanics: 1) the use associated to cyclic charge/discharge, and 2) the damage is due to deep discharges (under EoD limit). These two aging mechanics lead to an energy loss, which is directly reflected in the battery voltage, as it can be observed in Fig. 4a. As it can be seen in Fig. 4a the EoD was established in 3.2 V (red line) and the battery was subjected to deep discharges until reach 2.5 V. In addition, event thought the battery SoH decreases proportionally to the number of charges/discharges, the initial SoC does not present changes due to *memory effect* which causes the battery to store only the charge associated with the actual capacity C_T value. Additionally, the memory effect inhibits the visualization of the energy loss provoked by the aging [32]. On the other hand, the energy loss is the result of active materials transformation in inactive phases and leading to a reduction of battery capacity (*capacity loss*) at any discharge rate, and the increase of the battery impedance (*power fade*). Both capacity loss and power fade are related to the internal parameters of the battery. The capacity loss is evidenced by the reduction of the capacity C_T, and the power fade by the increase of the internal resistance R_{int} [33], and both phenomenas are proportional to the number of battery charge/discharge (N_{cycle}), as it can be seen in Fig. 4b-c. Furthermore, the variation of capacity and internal resistance make possible to quantify the aging level and consequently the battery End-of-Life (EoL).

Remark 1 The EoL determines when the battery has reached its useful life, and it could be associated to a specific SoH value, e.g in [34] it is reported that the life of a battery cell is ended when the maximum power of the cell decreases to 60% compared to its initial maximum power at the same operational conditions. In that sense, it can be assumed that a decrease of total capacity C_T and an increase of the internal resistance R_{int} of 0.6 (interpreted as 60%) determines the EoL of a cell. This EoL definition is established for a single battery cell, however it is possible to extend it for a battery made of several individual cells by assuming that the operational conditions and the aging behavior caused by the use are similar for all cells.

3.2 Modeling of Battery Degradation

In this work, the energy loss is modeled by considering the capacity loss and the power fade using experimental data. Both phenomena are related to number of charge/discharge cycles and modify the battery parameters in the system (18).

3.2.1 Capacity Loss Model

The Capacity loss model denoted as C_{loss} is defined by considering that the battery capacity (C_T) varies inversely proportionally according with the number of charges/discharges (N_{cycle}), and it is expressed as:

$$C_{loss}(N_{cycle}) = 1 - \frac{C_0 - C_T(N_{cycle})}{C_0}, \tag{24}$$

where C_0 is the initial capacity when the battery is new, $C_T(N_{cycle})$ is the capacity after each discharge cycle, $C_{loss}(N_{cycle}) \in \left[\, C_{loss}(EoL)\ 1 \,\right]$, i.e. when $C_{loss} = 1$ the battery is new and when $C_{loss}(EoL) \leq C_{loss} \leq 1$ the battery is in a degraded state. The result of Eq. 24 applied to experimental data presented in [35] is shown in Fig. 5a. As it can be noted, the capacity loss has a decrease of 0.4 (which can be also interpreted as a decrease of 40%) after 160 charge/discharge cycles, and it is occurs before it reaches

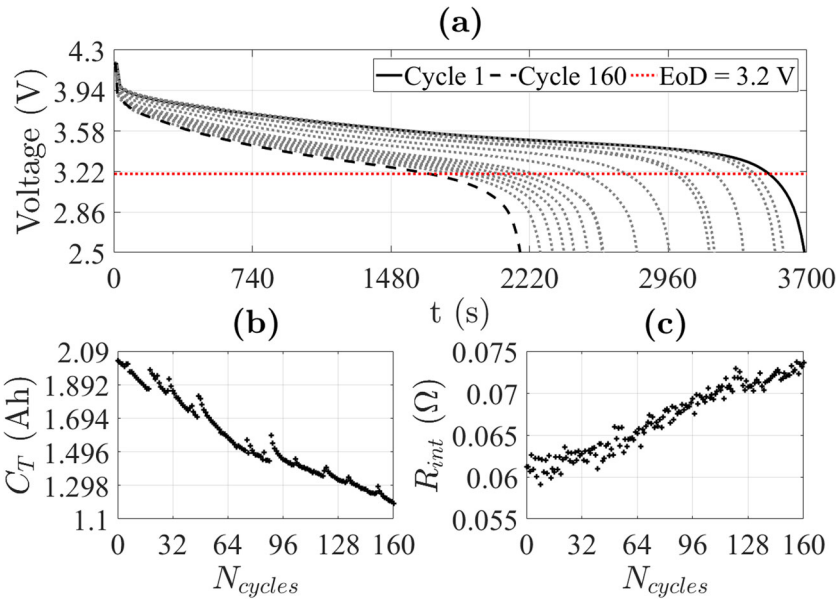

Fig. 4 **a** Voltage variation of a cell subjected to discharge cycles. **b** Evolution of capacity C_T and **c** Internal resistance R_{int} [35]

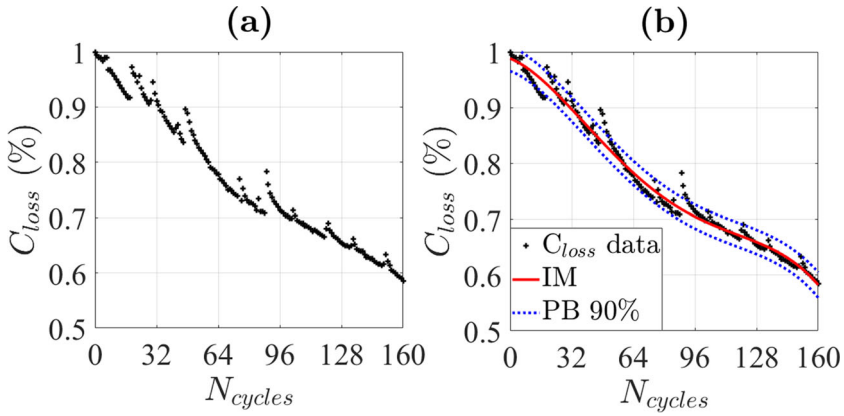

Fig. 5 **a** Evolution of Capacity loss C_T. **b** Identification of Capacity loss model

the EoL, i.e a SoH of 0.6 (60%) according to **Remark 1**. Then, using experimental data of capacity loss, a model is identified using a polynomial fourth-order equation and Prediction Bounds (PB) of 90% as:

$$IM_{C_{loss}}(N_{cycle}) = \sum_{i=0}^{4} \alpha_i \cdot N_{cycle}^i \tag{25}$$

where α denote the polynomial coefficients. The comparison between the identified model (25) and the experimental data are shown in Fig. 5b.

3.2.2 Power Fade Model

The power fade model is denoted as R_{inc}. If it is considered that the battery internal resistance R_{int} varies proportionally to the number of charges/discharges (N_{cycle}) is expressed as:

$$R_{inc}(N_{cycle}) = 1 - \frac{R_f - R_{int}(N_{cycle})}{R_f - R_0}, \tag{26}$$

where R_0 is the initial internal resistance when the battery is new, $R_{int}(N_{cycle})$ is the internal resistance after each discharge cycle, R_f is the value of the internal resistance when the battery has reached its End of Life (EoL). $R_{inc}(N_{cycle}) \in \left[0 \; R_{inc}(EoL)\right]$. In Fig. 6a the increase of the internal resistance computed by Eq. 26 is shown. As it can be noted the internal resistance has an increase of 0.4 (interpreted as a increase of 40%) after 160 charge/discharge cycles, and it is occurs before it reaches the EoL. Furthermore, R_f is established at 0.6 (60%) according to **Remark 1**.

For the degraded behavior computed by Eq. 26, a model is identified using a polynomial second-order equation:

$$IM_{R_{inc}}(N_{cycle}) = \sum_{i=0}^{2} \beta_i \cdot N_{cycle}^i \tag{27}$$

where β_i denote the polynomial coefficients. The comparison between the identified model (27) and the experimental data are shown in Fig. 6b. Finally, the total capacity C_T and the internal resistance R_{int} in system (17) are rewritten as:

$$\begin{aligned} C_T &= C_T(N_{cycle}) \cdot IM_{C_{loss}}(N_{cycle}) \\ R_{int} &= R_{int}(N_{cycle}) \cdot IM_{R_{inc}}(N_{cycle}). \end{aligned} \tag{28}$$

Remark 2 Models (25) and (27) are computed considering only the degraded behavior of a single battery cell, and both models are dependent on the number of charges/discharges cycles N_{cycle}. In that sense, for other batteries with different capacity C_T and internal resistance R_{int} values, it is possible

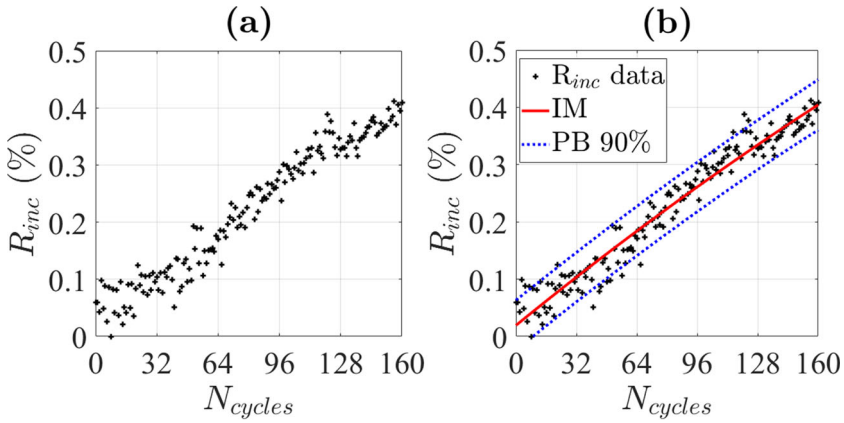

Fig. 6 **a** Evolution of increase of internal resistance R_{int}. **b** Identification of power fade model

to obtain similar degraded models, and the order of the polynomials was determined to best fit the experimental data (Table 1).

4 Path Planning Generation Algorithm

The path planning algorithm is defined considering two important aspects: (i) to guarantee the generation of smooth paths, i.e the position and orientation vary smoothly with the time avoiding aggressive maneuvers [36], and (ii) the maximization of flight endurance, i.e. the increase of the final flight time t_f. A smooth path could be associated to the system control inputs e.g a smooth evolution of the angular motor speed, and on the other hand, the maximization of flight endurance can be achieved by minimize the energy consumption during the flight. In order to make the link between a smooth path and a long flight endurance the path planning is introduced as a minimization of the total energy consumption and the final time.

4.1 Path Planning Based on Energy Consumption of an UAV Hexacopter

The energy provided by the battery is consumed entirely by the brushless DC motor and ESC. In that sense, the total energy consumption from initial time t_0 to final time t_f is computed as: [19, 36]:

$$E_c = \int_{t_0}^{t_f} [V_{batt} \cdot I_{batt}]dt = \int_{t_0}^{t_f} \sum_{m=1}^{N_m} [V_m \cdot I_m]dt, \tag{29}$$

where V_{batt} and I_{batt} are the battery voltage and the total current demanded by the BLDCMs. V_m and I_m are the voltage and current of each the BLDCM where $m \in [1, \cdots, N_m]$. N_m is the number of mth BLDCM in the hexacopter. By substituting Eqs. 21 and 22 in Eq. 29, the relationship between the energy consumption and angular speed of the BLDCMs is computed as:

$$E_c = \int_{t_0}^{t_f} \sum_{m=1}^{N_m} [\kappa_1 + \kappa_2\omega_m + \kappa_3\omega_m^2 + \kappa_4\omega_m^3 + \kappa_5\omega_m^4 + \kappa_6\dot{\omega}_m + \kappa_7\dot{\omega}_m^2 + \kappa_8\omega_m\dot{\omega}_m + \kappa_9\omega_m^2\dot{\omega}_m]dt, \tag{30}$$

where the constants $\kappa_1, \cdots, \kappa_8$ are combinations of the BLDCMs parameters, and ω_m and $\dot{\omega}_m$ are the speed and angular acceleration of the mth BLDCM. By considering that the initial and final speed are equals i.e $\omega_0 = \omega_f$ (30), can be simplified as:

$$E_c = \int_{t_0}^{t_f} \sum_{m=1}^{N_m} [\kappa_1 + \kappa_2\omega_m + \kappa_3\omega_m^2 + \kappa_4\omega_m^3 + \kappa_5\omega_m^4 + \kappa_6\dot{\omega}_m^2]dt, \tag{31}$$

The minimization of the energy consumption (31) and the mission final time tf is realized by defining a multi-objective constrained minimization problem taking into account the hexacopter dynamics and the constraints associated with the battery performance. In order to explain how is defined the minimization problem, let us consider Fig. 7, where the interaction of the different elements that integrate the dynamics of the hexacopter is shown. As it can be seen, the general inputs are the angular acceleration of the BLDCMs, considering the approach proposed by [19], and the output is the position and orientation of the hexacopter. Finally, the multi-objective constrained minimization problem is defined as follows:

$$\begin{aligned} \min_{\bar{\omega}_{r_i}} \quad & E_c(t_f)\&(t_f - t_0) \\ \textbf{such that} \quad & \text{Hexacopter dynamics (16)-(15)}, \\ & \text{BLDCM dynamics (20)-(21)-(22)}, \\ & \text{Battery dynamics (17)-(18)-(19)}, \\ & X_a(t_0) = X_{a_{t_0}},\ X_a(t_f) = X_{a_{t_f}}, \\ & 0 \le \omega_i \le \omega_{max}, \\ & V_{batt}(EoD) \le V_{batt}(t) \le V_{batt}(t_0), \\ & 0 \le SoH \le 1, \end{aligned} \tag{32}$$

where $X_a = \left[x\ \dot{x}\ y\ \dot{y}\ z\ \dot{z}\ \phi\ \dot{\phi}\ \theta\ \dot{\theta}\ \psi\ \dot{\psi}\ \omega_1\ \omega_2\ \omega_3\ \omega_4\ \omega_5\ \omega_6\ V_{SoH}\ V_d\ T_{batt}\right]^{\mathrm{T}}$ is the state vector with the dynamics of all the elements that integrate the hexacopter, ω_i is the speed of ith BLDCM, and $V_{batt}(EoD)$ is the battery voltage at End-of-Discharge value. In addition, the constraints associated with the BLDCMs speed and the battery voltage enable to set realistic operational limits. Moreover, the limit of

Table 1 Coefficients of identified models

Capacity loss model C_{loss}					
α_0	α_1	α_2	α_3	α_4	R^2
0.988	-1.406×10^{-3}	-6.713×10^{-5}	7.651×10^{-7}	-2.435×10^{-9}	0.98
Power loss model R_{inc}					
β_0	β_1	β_2	–	–	R^2
2.9×10^{-2}	4.027×10^{-3}	-2.604×10^{-6}			0.95

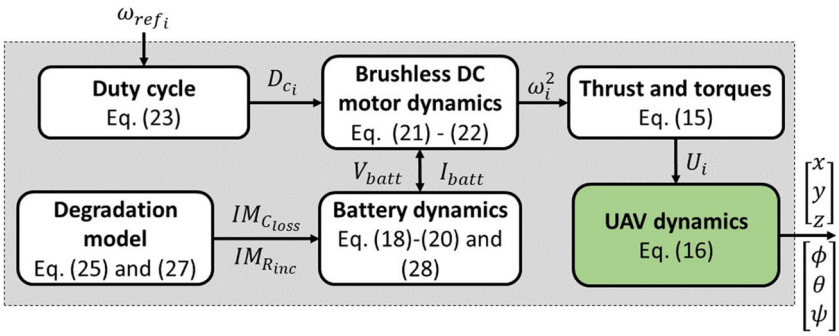

Fig. 7 Connection of UAV subsystems

minimal battery voltage, i.e. the End of Discharge, avoids to generate overdischarges.

4.2 Path Planning Based on Polynomial Functions

Polynomial functions are suitable for generating paths due to their properties such as smoothness and boundary conditions [35]. A polynomial function of n order is defined as:

$$\begin{aligned} p &= \sum_{i=0}^{n} \gamma_i t^i \\ &= \gamma_0 + \gamma_1 t + \cdots + \gamma_{2n-1} t^{2n-1}, \end{aligned} \tag{33}$$

where γ_i are the coefficients of polynomial and t is the time. The order determines the number of derivatives that must be resolved, i.e for $n = 3$ leads to minimum position and velocity path, and for $n = 5$ leads to smoother and minimum energy paths [21].

4.3 Orientation and Position Control Loops

A cascade control loop is considered in order to control and stabilize the position and orientation of the hexacopter. As it can be seen in Fig. 8, the control loop associated with the translational dynamics (external control loop or position controller) computes the reference thrust, denoted as $\bar{U}_1$ and Euler angles roll-θ_r and pith-θ_r. The reference of yaw-ψ_r is generated externally depending to path characteristics. The control loop associated to rotational dynamics (internal control loop or orientation controller) computes the reference torques, denoted as $\bar{U}_2$, $\bar{U}_3$, $\bar{U}_4$. Considering the system (23), a typical Proportional-Derivative (PD) controller is be defined for the hexacopter orientation as:

$$\begin{aligned} \bar{U}_2 &= (\phi_r - \phi)\, Kp_\phi - \dot{\phi} Kd_\phi, \\ \bar{U}_3 &= (\theta_r - \theta)\, Kp_\theta - \dot{\theta} Kd_\theta, \\ \bar{U}_4 &= (\psi_r - \psi)\, Kp_\psi - \dot{\psi} Kd_\psi \end{aligned} \tag{34}$$

where Kp_i and Kd_i corresponds to Proportional and Derivative gains and $i = \phi, \theta, \psi$. In the same way, the position controller is deduced as:

$$\begin{aligned} \phi_r &= (y_r(t) - y)\, Kp_y - \dot{y} Kd_y, \\ \theta_r &= (x_r(t) - x)\, Kp_x - \dot{x} Kd_x, \\ \bar{U}_1 &= \sigma((z_r - z) Kp_z - \dot{z} Kd_z) + g, \end{aligned} \tag{35}$$

where $\sigma = \frac{m}{\cos\phi \cos\theta}$, Kp_j and Kd_j corresponds to Proportional and Derivative gains and $j = x, y, z$. Moreover, $[\phi_r, \theta_r] \in \left[-\frac{\pi}{2}, \frac{\pi}{2}\right]$ and $-\pi \leq \psi_r \leq \pi$. The position reference $[x_r\ y_r\ z_r]^{\mathbb{T}}$ is computed using (33) for

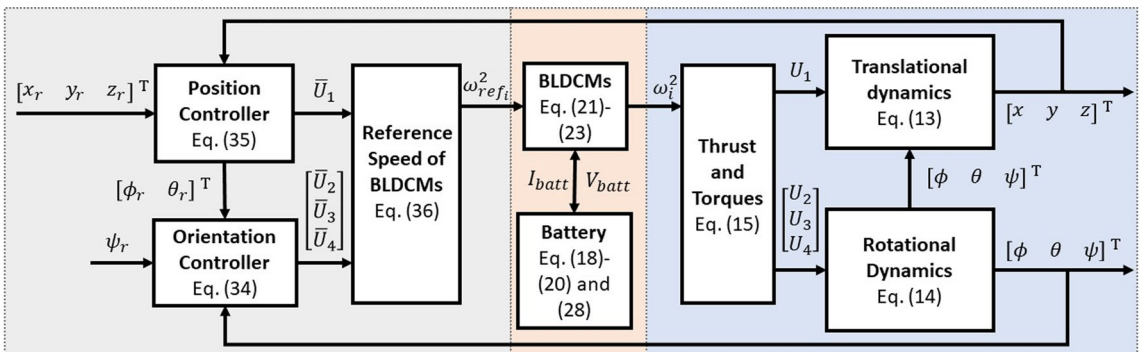

Fig. 8 Cascade control scheme

each axis. The reference speeds of the BLDCMs denoted as ω_{i_r} are deduced from Eq. 15 as:

$$\begin{bmatrix} \omega_{1_r}^2 \\ \omega_{2_r}^2 \\ \omega_{3_r}^2 \\ \omega_{4_r}^2 \\ \omega_{5_r}^2 \\ \omega_{6_r}^2 \end{bmatrix} = \begin{bmatrix} \frac{1}{6b} & 0 & -\frac{1}{3bl} & \frac{1}{6d} \\ \frac{1}{6b} & \frac{\sqrt{3}}{4bl} & -\frac{1}{6bl} & -\frac{1}{6d} \\ \frac{1}{6b} & \frac{\sqrt{3}}{4bl} & \frac{1}{6bl} & \frac{1}{6d} \\ \frac{1}{6b} & 0 & \frac{1}{3bl} & -\frac{1}{6d} \\ \frac{1}{6b} & -\frac{\sqrt{3}}{4bl} & \frac{1}{6bl} & \frac{1}{6d} \\ \frac{1}{6b} & -\frac{\sqrt{3}}{4bl} & -\frac{1}{6bl} & -\frac{1}{6d} \end{bmatrix} \begin{bmatrix} \bar{U}_1 \\ \bar{U}_2 \\ \bar{U}_3 \\ \bar{U}_4 \end{bmatrix}. \tag{36}$$

Finally, the duty cycle Dc_i for the ith-BLDCM is compute by considering the Eq. 22.

5 Simulation Results

The multi-objective constrained minimization problem (32) was solved using an optimal control software called GPOPS II which is a general-control software implemented in MATLAB®. It is dedicated to solve nonlinear optimal control problems using variable-order adaptive orthogonal collocation methods together with sparse nonlinear programming [37].

In order to test the capability of the path planning algorithm presented in Section 4.2 to minimize the energy consumption E_c and the final time t_f, two cases with the following boundary conditions were considered:

$$\begin{aligned} X_a(t_0) &= \left[0_{1\times 12},\ 454.7_{1\times 6},\ 1,\ 0,\ 25\right], \\ X_a(t_f) &= \left[x_f,\ 0,\ y_f,\ 0,\ z_f,\ 0_{1\times 5},\ \psi_f,\ 0,\ 454.7_{1\times 6},\right. \\ &\qquad \left. free,\ free,\ free\right]. \end{aligned} \tag{37}$$

In addition, the BLDCM speed was established as $\omega_i(t_0) = \omega_r(t_f) = 454.7$ rad/s taking into account the energy consumption criteria (31). Moreover, that initial speed makes it possible to generate the thrust force to take-off and remain lifted up during the flight.

5.1 Case 1

In the first case, the multi-objective constrained minimization problem (32) was solved considering a new ($SoH = 1$) and fully charged ($SoC = 1$) battery, $EoD = 12.8$ V. The minimal final time t_f was 7.0147 s. This final time was used in the polynomial approach to generate the path using the cascade control loop introduced in Section 4.3. In Figs. 9 and 10 the comparison between the minimum energy path generated by solving the minimization problem and the path generated by the polynomial approach is shown. As it can be seen, both methods generate similar smooth paths without aggressive maneuvers. However the difference between both methods can be observed in Fig. 11, where the minimization problem generate a very smooth transition between the initial and final orientation.

The battery response is shown in Figs. 12 and 13, as it can bee seen the demanded current for the minimization problem has an increase due to take off in comparison with the polynomial approach. This increase generates a considerable drop in battery voltage during takeoff (Fig. 12-b). The total consumed energy for the minimization problem and polynomial approach was 1.8657 kJ and 1.8772 kJ respectively. This result lets us to conclude that the minimization problem is capable of generating minimum energy paths, while at the same time minimizing the final time.

5.2 Case 2

To evaluate the minimization problem (32) in the present of a degraded battery, two changes in the battery SoH were considered at the beginning of the flight taking into account the boundary conditions (37): $SoH = 0.8077$, i.e a degradation of $\approx$ 20% at $N_{cycle} = 60$, and $SoH = 0.5946$, i.e. a degradation of $\approx$ 40% at $N_{cycle} = 160$.

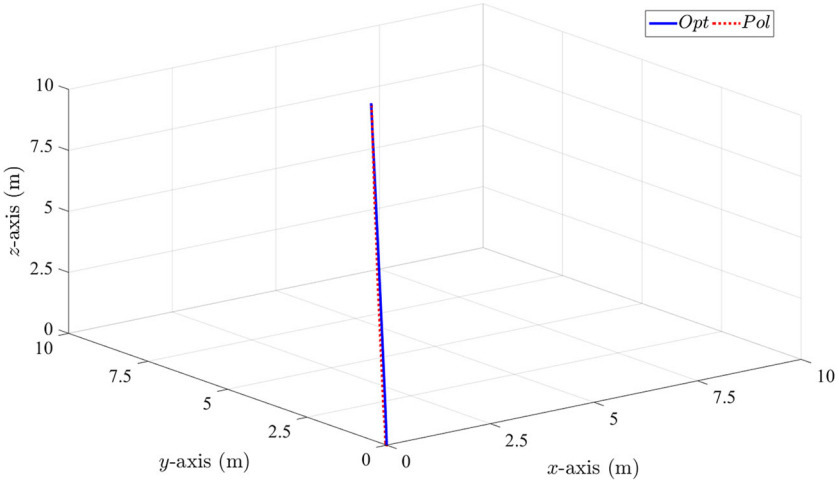

Fig. 9 Case 1: 3D Position around $x - y - z$ axis

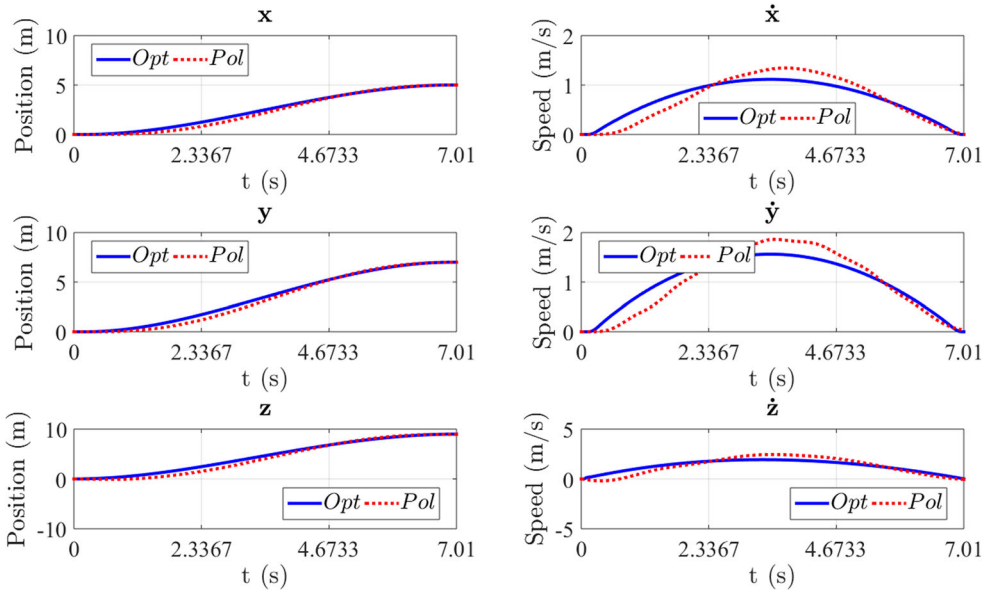

Fig. 10 Case 1: Position and linear speed around $x - y - z$ axis

As it can be seen in Figs. 14 and 15, the variation of the SoH battery modifies the final time value associated with the hexacopter mission (to see Table 2). That means, the consideration of battery health in the minimization problem not only enables to manage the issues associated with battery performance, it also defines the limits of flight endurance in order to determine if the available energy is sufficient to continue developing the mission. It can also be noted that the SoH variations also affects the discharge dynamics. As it can be seen in Fig. 16, to satisfy the requirement of minimum energy consumption and final time considering the performance index defined in Eq. 32, the discharge rate increase. On the other hand, it can be also notice that the initial SoC indicates that the battery is always fully charged at the beginning of the flight, but due to capacity loss and the final SoC tends to be rapidly decreasing.

Finally, the result of the minimization problem with SoH variation at 40% is compared with the response obtained by the polynomial approach in order to validate the result. As it is illustrated in Fig. 17, the minimization problem is able to compensate for the effects generated by the variation in the battery SoH generating an energy consumption of 2.4035 kJ and 2.5341 kJ for the polynomial approach.

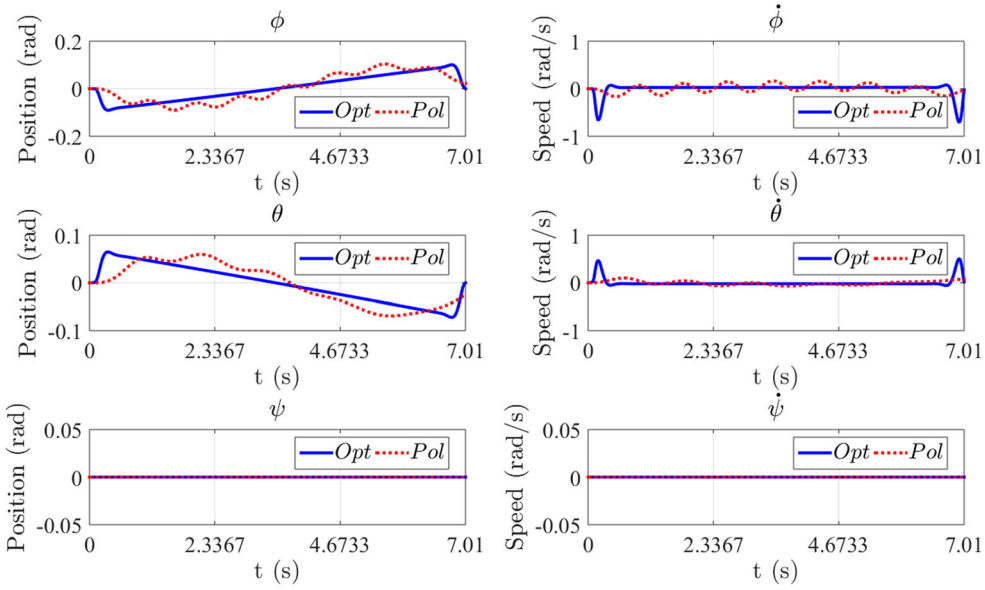

Fig. 11 Case 1: Orientation and angular speed around Euler angles $[\phi\, \theta\, \psi]$

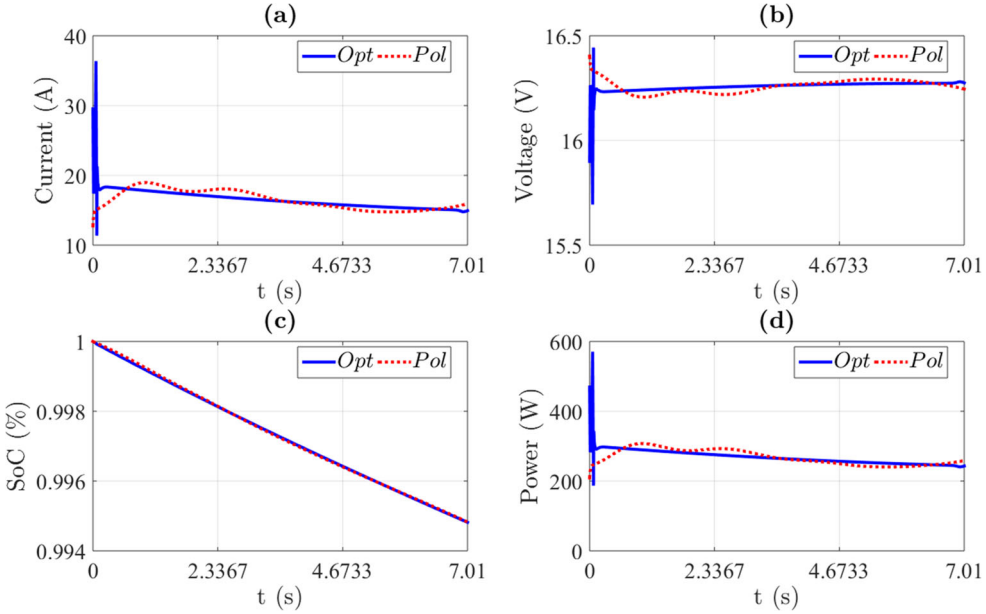

Fig. 12 Case 1: Battery response

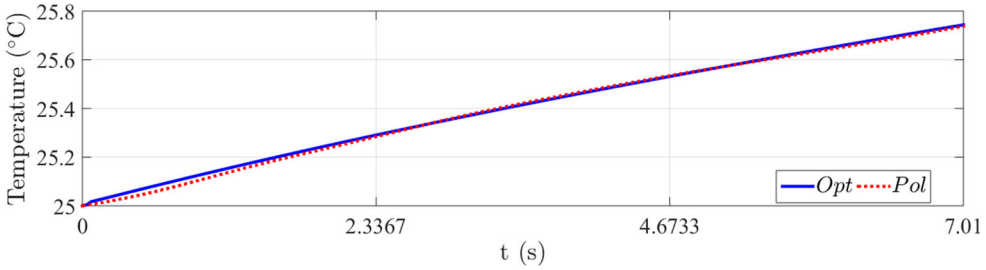

Fig. 13 Case 1: Battery temperature

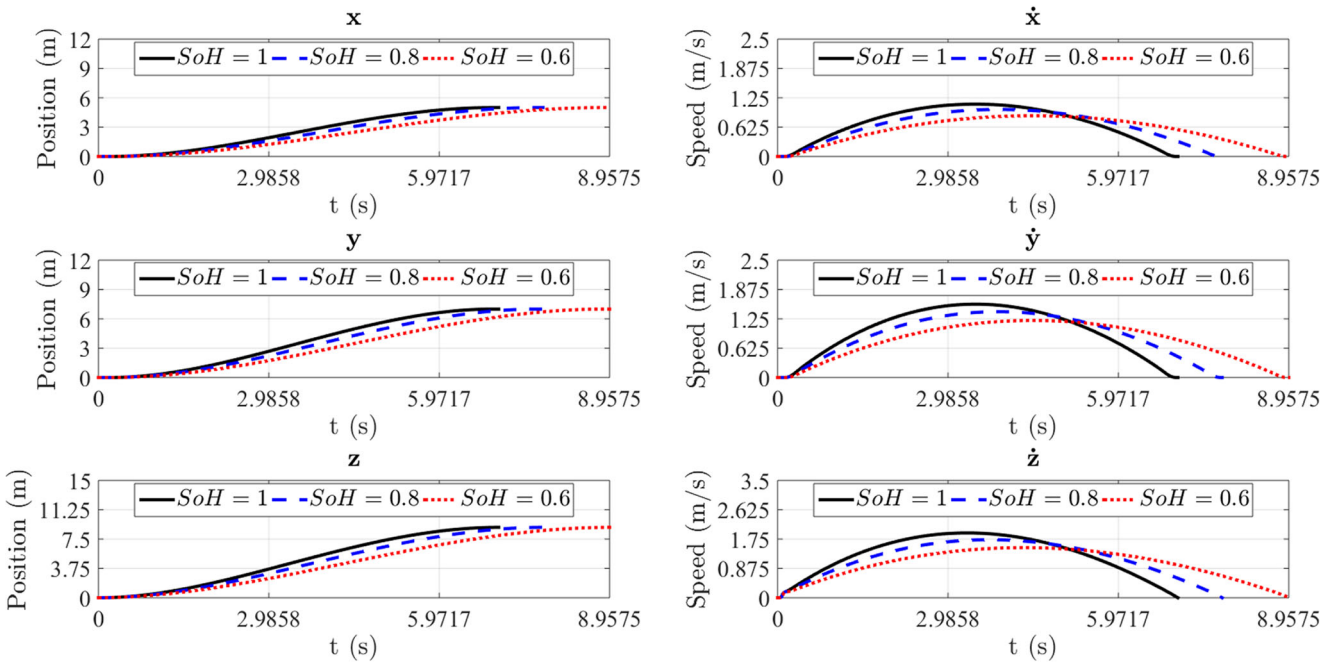

Fig. 14 Case 2: Position and linear speed around $x - y - z$ axis

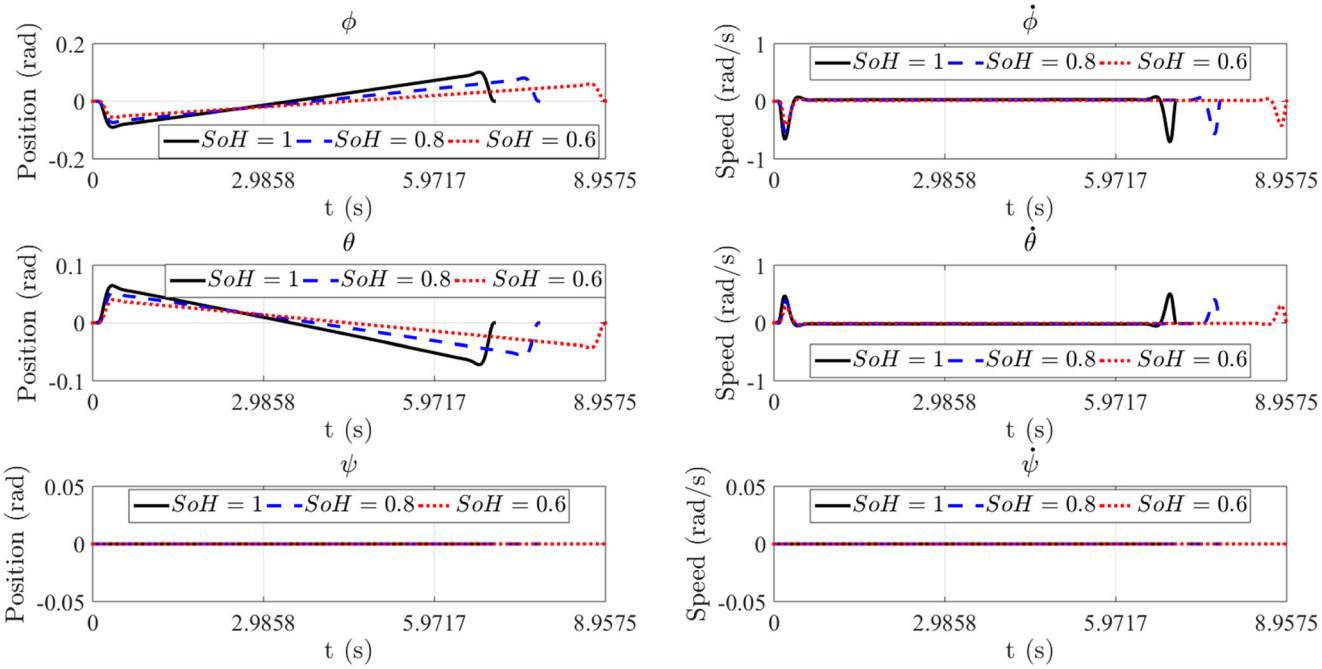

Fig. 15 Case 2: Hexacopter position and linear speed around $x - y - z$ axis

Table 2 Results of multi-objective minimization problem with SoH variations

t_f (s)	SoH (%)	N_{cycle}	$E_c(t_f)$ (kJ)
7.0147	100	0	1.8857
7.7908	80	60	2.0922
8.9575	60	160	2.4035

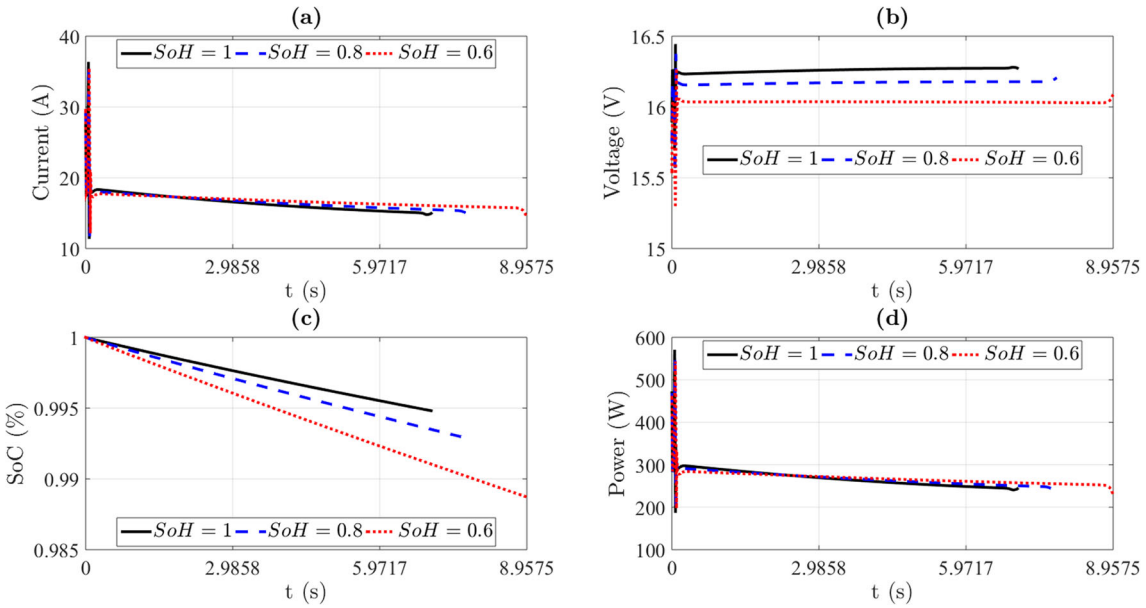

Fig. 16 Case 2: Battery response

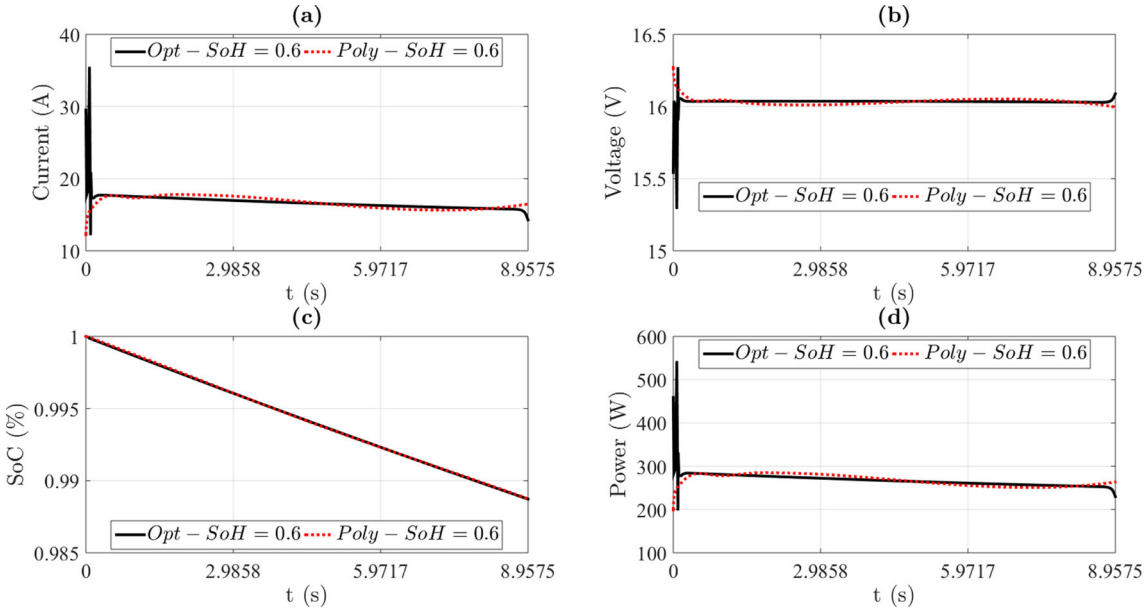

Fig. 17 Comparison of battery response between minimization problem and polynomial approach

6 Conclusions and Future Works

In this paper a path planning generation algorithm for a class of UAV multirotors was introduced as a multi-objective minimization problem associated to both energy consumption and final time by taking into account the battery performances. The battery performance was characterized by the State of Health, which was computed by introducing two degradation models associated with the number of charge/discharge cycles. On the other hand, a path generation approach based on polynomial functions was presented to validate the results obtained by the multi-objective minimization problem. The simulation results showed that it is possible to obtain a smooth and minimal energy path in the present of a degraded battery while minimizing the final time. In addition, the main challenge that the minimization problem has to overcome is the increases of the discharge rate due to energy loss. Considering the increase of the discharge rate, it is necessary to evaluate during the flight the energy available to determine if it is possible to continue and fulfill the mission avoiding overdischarges in the battery. Finally, as future works a more extensive study will be carried out to determinate the degradation models based on battery temperature. Furthermore, different flight sceneries taking into account the disturbance caused by the wind will be included in the minimization problem for paths characterized by several way-points.

Acknowledgements Ricardo Schacht Rodríguez acknowledges the economic support provided by Consejo Nacional de Ciencia y Tecnología (CONACyT) through doctoral scholarship program.

References

1. Possoch, M., Bieker, S., Hoffmeister, D., Bolten, A., Schellberg, J., Bareth, G.: Multi-temporal crop surface models combined with the RGB vegetation index from UAV-based images for forage monitoring in grassland. Int. Arch. Photogramm. Remote. Sens. Spat. Inf. Sci. **41**, 991 (2016)
2. Nex, F., Remondino, F.: UAV For 3D mapping applications: a review. Appl. Geomatics **6**(1), 1–15 (2014)
3. Fernández-Lozano, J., Gutiérrez-Alonso, G.: Improving archaeological prospection using localized UAVs assisted photogrammetry: an example from the Roman Gold District of the Eria River Valley (NW Spain). J. Archaeol. Sci. Rep. **5**, 509–520 (2016)
4. Stek, T.D.: Drones over mediterranean landscapes. The potential of small UAVs (drones) for site detection and heritage management in archaeological survey projects: a case study from Le Pianelle in the Tappino Valley, Molise (Italy). J. Cult. Herit. **22**, 1066–1071 (2016)
5. Nishar, A., Richards, S., Breen, D., Robertson, J., Breen, B.: Thermal infrared imaging of geothermal environments and by an unmanned aerial vehicle (UAV): a case study of the Wairakei-Tauhara geothermal field, Taupo, New Zealand. Renew. Energy **86**, 1256–1264 (2016)
6. Turner, I.L., Harley, M.D., Drummond, C.D.: UAVS for coastal surveying. Coast. Eng. **114**, 19–24 (2016)
7. Casella, E., Rovere, A., Pedroncini, A., Stark, C.P., Casella, M., Ferrari, M., Firpo, M.: Drones as tools for monitoring beach topography changes in the Ligurian Sea (NW Mediterranean). Geo-Mar. Lett. **36**(2), 151–163 (2016)
8. Tulum, K., Durak, U., Yder, S.K.: Situation aware UAV mission route planning. In: 2009 IEEE Aerospace conference, pp. 1–12 (2009)
9. MacAllister, B., Butzke, J., Kushleyev, A., Pandey, H., Likhachev, M.: Path planning for non-circular micro aerial vehicles in constrained environments. In: 2013 IEEE International Conference on Robotics and Automation (ICRA), pp. 3933–3940 (2013)

10. Bircher, A., Kamel, M., Alexis, K., Oleynikova, H., Siegwart, R.: Receding horizon path planning for 3D exploration and surface inspection. Auton. Robot. **42**(2), 291–306 (2018)
11. Nguyen, P.D., Recchiuto, C.T., Sgorbissa, A.: Real-time path generation and obstacle avoidance for multirotors: a novel approach. J. Intell. Robot. Syst. **89**(1-2), 27–49 (2018)
12. Quionez, Y., Barrera, F., Bugueo, I., Bekios-Calfa, J.: Simulation and path planning for quadcopter obstacle avoidance in indoor environments using the ROS framework. In: International Conference on Software Process Improvement, pp. 295–304 (2017)
13. Richter, C., Bry, A., Roy, N.: Polynomial trajectory planning for aggressive quadrotor flight in dense indoor environments. In: Inaba M., Corke P. (eds) Robotics Research. Springer Tracts in Advanced Robotics, vol 114. Springer, Cham (2016)
14. Cheng, F., Hua, W., Pin, C.: Rotorcraft flight endurance estimation based on a new battery discharge model. Chin. J. Aeronaut. **30**(4), 1561–1569 (2017)
15. Broussely, M., Biensan, P., Bonhomme, F., Blanchard, P., Herreyre, S., Nechev, K., Staniewicz, R.: Main aging mechanisms in Li-Ion batteries. J. Power Sources **146**(1-2), 90–96 (2005)
16. Pounds, P., Mahony, R., Gresham, J., Corke, P., Roberts, J.M.: Towards dynamically favourable quad-rotor aerial robots. In: Proceedings of the 2004 Australasian Conference on Robotics & Automation, Australian Robotics & Automation Association (2004)
17. Driessens, S., Pounds P.E.: Towards a more efficient quadrotor configuration. In: 2013 IEEE/RSJ International Conference on Intelligent Robots and Systems (IROS), pp. 1386–1392 (2013)
18. Verbeke, J., Hulens, D., Ramon, H., Goedeme, T., De Schutter, J.: The design and construction of a high endurance hexacopter suited for narrow corridors. In: 2014 International Conference on Unmanned Aircraft Systems (ICUAS), pp. 543–551 (2014)
19. Morbidi, F., Cano, R., Lara, D.: Minimum-energy path generation for a quadrotor UAV. In: 2016 IEEE International Conference on Robotics and Automation (ICRA), pp. 1492–1498 (2016)
20. Dietrich, T., Krug, S., Zimmermann, A.: An empirical study on generic multicopter energy consumption profiles. In: 2017 Annual IEEE International Systems Conference (SysCon), pp. 1–6 (2017)
21. Kreciglowa, N., Karydis, K., Kumar, V.: Energy efficiency of trajectory generation methods for stop-and-go aerial robot navigation. In: 2017 International Conference on Unmanned Aircraft Systems (ICUAS), pp. 656–662 (2017)
22. Chamseddine, A., Zhang, Y., Rabbath, C.A., Join, C., Theilliol, D.: Flatnessbased trajectory planning/replanning for a quadrotor unmanned aerial vehicle. IEEE Trans. Aerosp. Electron. Syst. **48**(4), 2832–2848 (2012)
23. Carrillo, L.R.G., LÓpez, A.E.D., Lozano, R., Pégard, C.: Quad Rotorcraft Control: Vision-Based Hovering and Navigation. Springer, Berlin (2012)
24. Ortiz-Torres, G., García-Beltrán, C.D., Reyes-Reyes, J., Vidal-Rosas, A., Astorga Zaragoza, C.: Control Tolerante a Fallas Pasivo de un Octorotor tipo X8 utilizando Controladores Backstepping en Cascada, XVI convención de ingeniería eléctrica, CIE, pp. 1–8 (2015)
25. Gargioli, A., Rinaldi, F., Quagliotti, F.: Proportional Integral Derivative and Linear Quadratic Regulation of a multirotor attitude: mathematical modelling, simulations and experimental results. In: 2013 International Conference on Unmanned Aircraft Systems (ICUAS), pp. 433–442 (2013)
26. Julien, C., Mauger, A., Vijh, A., Zaghib, K.: Lithium Batteries, pp. 29–68. Springer, Berlin (2016)
27. Chen, M., Rincon-Mora, G.A.: Accurate electrical battery model capable of predicting runtime and IV performance. IEEE Trans. Energy Conversion **21**(2), 504–511 (2006)
28. Bø, T.I., Johansen, T.A.: Battery power smoothing control in a marine electric power plant using nonlinear model predictive control. IEEE Trans. Control Syst. Technol. **25**(4), 1449–1456 (2017)
29. El-Samahy, A.A., Shamseldin, M.A.: Brushless DC motor tracking control using self-tuning fuzzy PID control and model reference adaptive control. Ain Shams Engineering Journal, In Press, Corrected Proof (2016)
30. Moseler, O., Isermann, R.: Application of model-based fault detection to a brushless DC motor. IEEE Trans. Ind. Electron. **47**(5), 1015–1020 (2000)
31. Sasaki, T., Ukyo, Y., Novák, P.: Memory effect in a lithium-ion battery. Nat. Mater. **12**(6), 569 (2013)
32. Cordoba-Arenas, A., Onori, S., Rizzoni, G., Fan, G.: Aging propagation in advanced battery systems: preliminary results. IFAC Proc. **46**(21), 313–318 (2013)
33. Haifeng, D., Xuezhe, W., Zechang, S.: A new SoH prediction concept for the power Lithium-Ion battery used on HEVs. In: 2009 IEEE VPPC09 Conference ON Vehicle Power and Propulsion, pp. 1649–1653 (2009)
34. Saha, B., Goebel, K.: Battery data set NASA AMES prognostics data repository (2007)
35. Corke, P.: Robotics, Vision and Control: Fundamental Algorithms In MATLAB® Second Completely Revised, vol. 118. Springer, Berlin (2017)
36. Tokekar, P., Karnad, N., Isler, V.: Energy-optimal trajectory planning for car-like robots. Auton. Robot. **37**(3), 279–300 (2014)
37. Patterson, M.A., Rao, A.V.: GPOPS-II: a MATLAB software for solving multiple-phase optimal control problems using hp-adaptive gaussian quadrature collocation methods and sparse nonlinear programming. ACM Transactions on Mathematical Software (TOMS) **41**(1), 1 (2014)

R. Schacht-Rodríguez received his M. Sc. degree in Electronic Engineering specializing in Automatic Control in 2015 from Centro Nacional de Investigación y Desarrollo Tecnológico (Cuernavaca, México). In 2012 he received the B. S. degree in Mechatronics Engineering specializing in Process Control from the Instituto Tecnológico Superior de Coatzacoalcos (Coatzacoalcos México). He is currently doing his Ph. D. studies in a co-direction agreement between the Centro Nacional de Investigación y Desarrollo Tecnológico, (Cuernavaca, Mexico) and the Research Centre for Automatic Control of Nancy (CRAN) at University of Lorraine (Nancy, France). His main areas of research are the Model-based Prognosis & Fault Diagnosis, and the development of control and path planning strategies based on energy of Unmanned Aerial Vehicles.

J.-C. Ponsart is full professor in the Research Centre for Automatic Control of Nancy (CRAN) at University of Lorraine (Nancy, France). He received the Ph.D. degree in 1996 from University of Savoie (Annecy, France) in Control Engineering (nonlinear control of magnetic suspensions and its digital implementation aspects). In 1997, he participated in the design and implementation of real-time controllers with digital signal processor architecture for an industrial company. He received his Habilitation à Diriger des Recherches in 2011 from the University of Lorraine in Model-based Fault Tolerant Control and Application to a Winding Machine. His current research interests include sensor and actuator model-based fault diagnosis (FDI) method synthesis and active fault-tolerant control (FTC) system design for LTI, LPV, nonlinear systems. He published over 90 journal/conference papers and is co-author of a book untitled Fault-tolerant Control Systems: Design and Practical Applications.

C.-D. García-Beltrán received his professional diploma in Electronics Engineering from the San Luis Potosí University, México, in 1992, an M.Sc. degree in Electronic Engineering from the Centro Nacional de Investigación y Desarrollo Tecnológico (CENIDET), Cuernavaca, Morelos, México, in 1997, and a Ph.D. degree in Engineering from the INPG, France, in 2004. He is currently professor of department of electronic engineering at the CENIDET. His research areas are intelligent control, fault diagnosis, fault tolerant control and embedded control systems.

C.-M. Astorga-Zaragoza was born in Minatitlán, Veracruz, México in 1967. He is an Electronic Engineer graduated in 1990 from the Instituto Tecnológico de Minatitlán, Veracruz, México. He received the degree of Master of Science in Electronic Engineering at the National Center for Research and Technological Development (CENIDET), Cuernavaca, Morelos, Mexico, in 1993, and the degree of Doctor of Process Engineering at the University of Lyon 1 in France October 2001. In 2009, held a postdoc in Automatic Control at the University of Nancy 1 in France.

D. Theilliol received the Ph.D. degree in Control Engineering from UNIVERSITY OF LORRAINE (France) in 1993. Since September 2004, he is a full Professor in Research Centre for Automatic Control of Nancy (CRAN) at University of Lorraine where he co-ordinates and leads national, European and International R&D projects in steel industries, wastewater treatment plant and aerospace domains. His current research interests include sensor and actuator model based fault diagnosis (FDI)method synthesis and active fault tolerant control (FTC) system design for LTI, LPV, Multilinear systems and also reliability analysis of components. Prof. Theilliol published over 200 journal/conference papers and is a co-author of a book entitled 'Fault-tolerant Control Systems: Design and Practical Applications (2009). He was during two years Visiting Professorship for Senior International Scientists for Chinese Academy of Sciences.He is one of European Advanced Control and Diagnosis (EACD) steering committee members and is also a member of IFAC Technical Committee 6.2.Mining, Mineral and Metal Processing.

Y. Zhang (M'99–SM'07) received the B.S., M.S., and Ph.D. degrees in automatic controls from the Northwestern Polytechnical University, Xi' an, China, in 1983, 1986, and 1995, respectively. He is currently a Professor at the Department of Mechanical, Industrial and Aerospace Engineering, Concordia University, Montreal, QC, Canada. He has authored four books, more than 460 journal and conference papers, and book chapters. His current research interests include fault diagnosis and fault-tolerant (flight) control systems, cooperative GNC of unmanned aerial/space/ground/surface vehicles. Dr. Zhang is a Fellow of CSME, a Senior Member of AIAA, the Vice- President of International Society of Intelligent Unmanned Systems, and a member of the Technical Committee for several scientific societies. He is an Editorial Board Member, Editor-in-Chief, Editor-at-Large, and Editor or Associate Editor of several international journals. He has served as the General Chair, the Program Chair, and IPC Member of several international conferences.

Affiliations

R. Schacht-Rodríguez[1,2] · J.-C. Ponsart[2] · C.-D. García-Beltrán[1] · C.-M. Astorga-Zaragoza[1] · D. Theilliol[2] · Y. Zhang[3]

R. Schacht-Rodríguez
rschacht@cenidet.edu.mx;
ricardo.schacht-rodriguez@univ-lorraine.fr

C.-D. García-Beltrán
cgarcia@cenidet.edu.mx

C.-M. Astorga-Zaragoza
astorga@cenidet.edu.mx

D. Theilliol
didier.theilliol@univ-lorraine.fr

Y. Zhang
youmin.zhang@concordia.ca

[1] Tecnológico Nacional de México, Centro Nacional de Investigación y Desarrollo Tecnológico (cenidet), Cuernavaca, Morelos, México

[2] Centre de Recherche en Automatique de Nancy (CRAN - CNRS UMR 7039), Université de Lorraine, Vandoeuvre-Les-Nancy, France

[3] Department of Mechanical, Industrial and Aerospace Engineering, Concordia University, Montreal, Quebec H3G 1M8, Canada